

GHOST ON THE SHELL: AN EXPRESSIVE REPRESENTATION OF GENERAL 3D SHAPES

Zhen Liu^{1,2} Yao Feng^{1,3,*} Yuliang Xiu^{1,*} Weiyang Liu^{1,4,†} Liam Paull² Michael J. Black^{1,‡} Bernhard Schölkopf^{1,‡}

¹Max Planck Institute for Intelligent Systems - Tübingen ²Mila, Université de Montréal ³ETH Zürich

⁴University of Cambridge *Equal contribution †Directional lead ‡Shared last author

Project Page: gshell3d.github.io

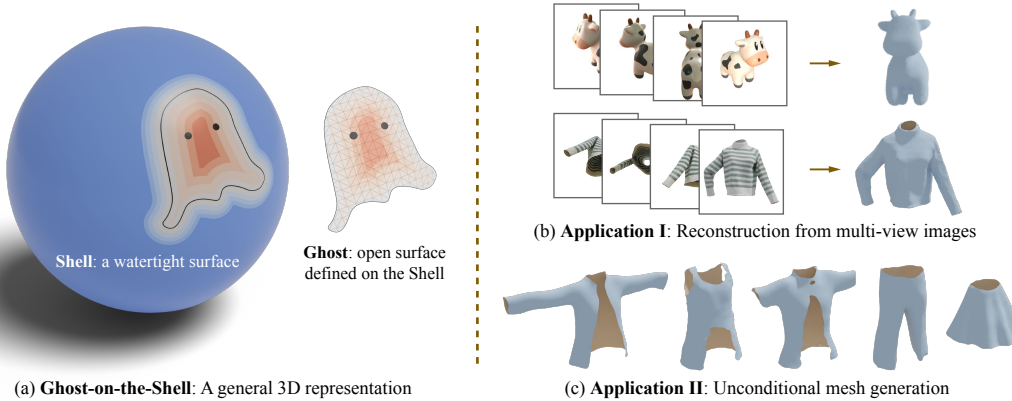


Figure 1: Left: Illustration of mesh extraction with **G-SHELL** through a manifold signed distance on a surface; Right: Applications of **G-SHELL**, multiview mesh reconstruction (top) and mesh generation (bottom).

ABSTRACT

The creation of photorealistic virtual worlds requires the accurate modeling of 3D surface geometry for a wide range of objects. For this, meshes are appealing since they 1) enable fast physics-based rendering with realistic material and lighting, 2) support physical simulation, and 3) are memory-efficient for modern graphics pipelines. Recent work on reconstructing and statistically modeling 3D shape, however, has critiqued meshes as being topologically inflexible. To capture a wide range of object shapes, any 3D representation must be able to model solid, watertight, shapes as well as thin, open, surfaces. Recent work has focused on the former, and methods for reconstructing open surfaces do not support fast reconstruction with material and lighting or unconditional generative modelling. Inspired by the observation that open surfaces can be seen as islands floating on watertight surfaces, we parameterize open surfaces by defining a manifold signed distance field on watertight templates. With this parameterization, we further develop a grid-based and differentiable representation that parameterizes both watertight and non-watertight meshes of arbitrary topology. Our new representation, called *Ghost-on-the-Shell* (**G-SHELL**), enables two important applications: differentiable rasterization-based reconstruction from multiview images and generative modelling of non-watertight meshes. We empirically demonstrate that **G-SHELL** achieves state-of-the-art performance on non-watertight mesh reconstruction and generation tasks, while also performing effectively for watertight meshes.

1 INTRODUCTION

The creation of high-fidelity 3D virtual worlds requires a representation of 3D shape that can be rendered and simulated efficiently and realistically. Most commonly, 3D shapes are represented as meshes for which modern graphics pipelines are highly optimized. Because the manual creation of 3D mesh assets is time-consuming, research has focused on the automatic creation from images or generative models. While much of the recent work has focused on watertight meshes [50, 51, 55, 61],

many 3D objects, such as clothing, paper or leaves, are non-watertight, open¹ and thin. The capture and generative modeling of such surfaces is relatively underexplored.

Existing modeling methods for non-watertight meshes typically build an unsigned distance field (UDF) [34, 37], a scalar field of the absolute distances of 3D coordinates to the nearest surface. With UDF, one may obtain non-watertight meshes by extracting and discretizing the zero UDF levelset. However, isosurface extraction from a UDF, compared to that of signed distance fields (SDF), is a non-trivial task: the bisection search strategy in classical algorithms such as Marching Cubes [38] does not simply apply to UDFs. Common workarounds include 1) post-processing double-layered watertight mesh [45, 64], introducing local pseudo-signs for bisection search [14], and using implicit-free point-to-mesh reconstruction methods [10]. These methods inevitably introduce modeling errors, posing a challenge for non-watertight mesh reconstruction and generation.

We take a different approach to modeling non-watertight meshes with the following key observation – most open surfaces can be viewed as entities floating on watertight surfaces, analogous to continents floating on the Earth’s surface. In other words, it suffices to model the open surface boundary on some watertight surface template. To formalize this idea, we define a manifold signed distance field (mSDF) on the watertight template, in which the sign indicates whether a point lies in the open surface or not, and the absolute scale indicates the geodesic distance to the boundary. An open surface can now be extracted via isoline extraction with mSDF.

We follow this intuition and design a general representation, *Ghost-on-the-Shell* (dubbed **G-SHELL**), which jointly parameterizes the watertight template and the non-watertight mesh living on it. Specifically, we discretize the 3D space into a grid of cells, of which the vertices store both SDF and mSDF values, and then apply Marching-Cubes-like extraction to obtain the SDF isosurface and the mSDF isoline. Our implementation exploits an efficient mesh extraction algorithm instead of following the naïve two-stage approach of “isosurface to isoline”. In a nutshell, we adapt the look-up table in Marching-Cubes-like algorithms, which enumerate all possible configurations of isosurfaces in each cell according to both SDF and mSDF signs. Such an implementation effectively reduces the number of mesh faces created and thus the computational cost of the grid-to-mesh mapping.

Since **G-SHELL** uses only simple, deterministic and parallelizable operations for mesh extraction, mesh-based inverse rendering can now be applied to non-watertight meshes due to nicely-behaved optimization landscapes (with simple Marching-Cubes-like extraction) and memory-friendly computation (with efficient mesh rasterizers). This efficient mesh rasterization means that we are now able to optimize both material and lighting from pixel information by exploiting physics-based rendering of meshes. Furthermore, the regular grid structure of **G-SHELL** allows the extension of recent generative methods, such as diffusion models, to non-watertight meshes for the first time.

In summary, our major contributions are listed below:

- **Mesh representation.** **G-SHELL** is a differentiable representation that effectively parameterizes both watertight and non-watertight meshes of different shape topologies.
- **Efficiency.** With the designed mesh extraction algorithm for **G-SHELL**, we achieve fast reconstruction of non-watertight meshes with differentiable rasterizers. Specifically, we design an efficient mesh extraction algorithm for **G-SHELL**.
- **Physics-based inverse rendering.** **G-SHELL** enables joint optimization of topology, material, and lighting of both watertight and non-watertight meshes.
- **Mesh generation.** The grid parameterization and efficient mesh extraction of **G-SHELL** enables effective generative modeling of both watertight and non-watertight meshes with diffusion models.
- We qualitatively and quantitatively compare **G-SHELL** with current popular 3D representations on reconstruction from realistic images and unconditional generation of both watertight and non-watertight meshes, demonstrating the superiority of **G-SHELL** in representing 3D shapes.

2 RELATED WORK

Mesh parameterization and extraction. In contemporary computer graphics pipelines and software, 3D meshes serve as a crucial and foundational representation. The means of mesh reconstruction can mostly be classified into three categories: from mesh templates, from point clouds and from implicit

¹i.e., bordered. Not to be confused with the mathematical term of openness.

fields. Mesh templates enable the optimization of vertex positions to align with object surfaces but can be inflexible for diverse topologies [15, 59]. Some methods [43, 54, 56] utilize remeshing [5, 19] to accommodate topology changes, but careful initialization remains essential to avoid bad local minima during optimization. Point clouds, compared to mesh templates, can be directly obtained from Lidar scans and at the same time offer flexibility in capturing diverse shape topologies. Such flexibility comes at the cost of the challenge in inferring point connectivity – whether two points are adjacent to each other on the target surface. Common methods for building surfaces from point clouds, such as Ball-Pivoting [3] and Delaunay Triangulation [27], are not only slow due to non-parallelizable operations but susceptible to noises in source point clouds.

It is therefore more common to extract meshes from implicit fields, which may be built from point clouds with Poisson reconstruction [23, 44, 49], or from multiview images [40, 61]. Subsequently, meshes can be extracted by identifying and triangulating the zero levelsets with methods like Marching Cubes [38], Marching Tetrahedra [53] and Dual Contouring [22]. Many of these mesh extraction algorithms are made differentiable, such as in Deep Marching Cubes [29], Neural Dual Contouring [9], MeshSDF [46], DMTet [50] and FlexiCubes [51]. However, most of these differentiable methods only apply to watertight meshes due to the use of signed distance fields (SDFs). To handle non-watertight meshes, some papers propose differentiable methods using unsigned distance field. For instance, MeshUDF [14] computes pseudo-signs on grid vertices – the signs of inner products between UDF gradients on grid vertices – and reuse Marching Cubes to extract meshes from the resulted pseudo SDFs. These methods are sensitive to input noises, due to the challenge in accurately identifying zero levelsets from non-negative fields. In comparison, our method could robustly model the non-watertight mesh since the zero levelset is extracted from general real-valued fields instead.

Differentiable inverse rendering. It is popular in recent years to perform differentiable inverse rendering through implicit representations, such as NeRF [40] and SDF [55, 61], with which one may utilize differentiable volumetric rendering [36, 40] or surface rendering [21, 31, 61] methods. These methods are adapted to reconstruct non-watertight surfaces with UDF (e.g., NeuralUDF [37], NeUDF [34]) and SDF (e.g., NeAT [39]). However, rendering with implicit representations typically requires multiple and likely expensive queries for each pixel in the rendered image. And since the geometry and color are encoded in an implicit way, it is relatively hard to disentangle geometry, material and lighting during inverse rendering. In contrast, explicit representations, such as point clouds and meshes, can be efficiently rendered with rasterization [24, 32], and allow easy disentanglement of physical properties [16, 33, 41]. Compared to the implicit-based methods for non-watertight mesh modeling, our method takes advantage of mesh-based rasterization to enable fast joint optimization of shapes, materials and lighting from multi-view images.

Generative modeling of geometry. 3D generation is widely studied for various representations, including explicit representations like mesh [11, 12, 35, 42], point clouds [60, 62], voxels [57], and implicit ones like signed distance functions (SDFs) [6, 63] and neural radiance fields (NeRF) [6, 7, 25, 48]. However, apart from few mesh-based methods, all the other ones do not directly generate meshes with arbitrary topology. As a result, one typically has to perform additional post-processing steps to extract meshes, which can be time-consuming and may introduce additional errors.

More recently, methods have been proposed to generate meshes using intermediate grid representations either through direct 3D modeling [11, 12, 35] or through lifting information from 2D generative models [8, 30]. While these methods achieve success in generating watertight 3D meshes, none of them can generate non-watertight meshes. It is also possible to directly generate meshes in an autoregressive way: for instance, PolyGen [42] builds a transformer-based autoregressive model to alternately produce vertices and edges. However, autoregressive models can be so flexible that they hardly scale to complex meshes with a very dense set of vertices and often produce self-intersecting meshes. Our method, instead, is capable of generating both watertight and non-watertight meshes with fine geometric details and without self-intersections.

3 PRELIMINARIES: SDF-BASED MESH EXTRACTION

We briefly summarize Marching Cubes, a classical SDF-based mesh extraction method, and introduce some of its variants. In a nutshell, Marching Cubes discretizes the 3D space with a 3D cubic grid and extracts faces from each cubic cell with a simple linear assumption: the SDF value of any point in each cell is a barycentric interpolation of those on cell corners. Specifically, given any point x in a cell with 8 corners (p_1, p_2, \dots, p_8), we first obtain the barycentric coordinate (c_1, c_2, \dots, c_8) such

that $x = \sum_i c_i p_i$. Under the linear assumption, the extracted mesh must be polygons with their vertices on the cubic cell edges. Therefore, it suffices to compute the mesh vertex position p' on each edge (p_i, p_j) with SDF values $s_i < 0 < s_j$, respectively. The vertex position is simply a linear interpolation between p_i and p_j : $u = (s_i p_j - s_j p_i)/(s_i - s_j)$.

The connectivity of these extracted mesh vertices can be efficiently inferred through a look-up table. One may instead use tetrahedral grids, leading to the variant called Marching Tetrahedra, for which we visualize the look-up table in Figure 2. Since the vertices are computed through simple differentiable operations, one may parameterize watertight meshes with a potentially deformable grid of SDF values – essentially deep marching cubes (with some relaxation) [29] and DMTet [50].

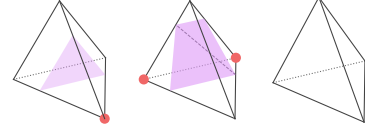


Figure 2: Look-up table for Marching Tetrahedra (up to rotation symmetry). Grid vertices with and without a red dot possess SDF values of opposite signs.

4 G-SHELL: AN EXPRESSIVE REPRESENTATION OF GENERAL 3D SHAPES

4.1 OPEN SURFACE LIVING ON WATERTIGHT SURFACE

We start with the following simple observation on a category of open surfaces, which guides our insight to parameterize general 3D shapes with open surfaces that live on a watertight surface.

Any smooth and simply-connected open surface can be smoothly deformed to be a subset of a sphere.

This is a direct consequence of classical topological theories on surfaces, of which more mathematical details are given in Appendix A. Indeed, a large number of surfaces (*e.g.*, plain T-shirts) can be completed to a watertight surface by first contracting the holes and later deforming it into a sphere. Inspired by this observation, we define a continuous and differentiable mapping $\nu : \mathcal{M} \rightarrow \mathbb{R}$ on the template sphere \mathcal{M} to characterize if a point belongs to the open surface \mathcal{M}_o :

$$\underbrace{\nu(x) > 0, \forall x \in \text{Interior}(\mathcal{M}_o)}_{\text{Case 1: inside the open surface}}, \quad \underbrace{\nu(x) = 0, \forall x \in \partial \mathcal{M}_o}_{\text{Case 2: on the surface boundary}}, \quad \underbrace{\nu(x) < 0, \text{Otherwise}}_{\text{Case 3: outside the open surface}}$$

where ν can be instantiated as the signed geodesic distance to the open surface boundary living on the watertight template. While the number of choices of ν given some \mathcal{M} and \mathcal{M}_o can be infinite, without loss of generality we call the field of ν manifold signed distance field (mSDF), since it is defined on a manifold surface and characterizes the boundary in a way that is similar to SDF.

The problem now effectively reduces to learning a “2D mesh” defined by the zero isoline of ν . Just as 3D meshes on the zero isosurface can be parameterized by 3D cubic grids in deep marching cubes, the “2D mesh” can also be parameterized by a “2D grid”, *i.e.*, the mesh for the (deformed) sphere: simply to learn a ν value on each of the sphere mesh vertices from which we extract non-watertight meshes. This process is illustrated in Figure 3. Intuitively speaking, an open surface can now be viewed as the remaining essence after cutting out the hollow vacuum on a 3D shell, and hence we name the proposed 3D representation Ghost-on-the-Shell².

Such a naïve construction, however, poses modeling challenges when applied to general objects. First, it cannot capture watertight surfaces that are not homeomorphic to spheres (*e.g.*, donuts). Furthermore, some naïve deformation of a surface in 3D may result in self-intersection and therefore addressing this requires additional regularization and/or modeling techniques.

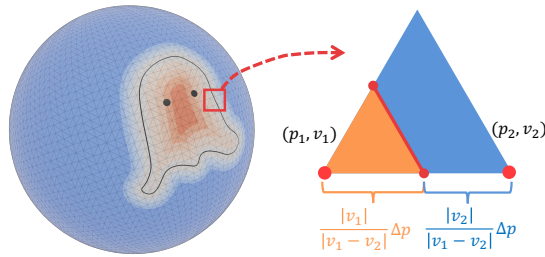


Figure 3: Illustration of non-watertight mesh extraction from some watertight triangular mesh. p_1, p_2 are the positions of (watertight) mesh vertices. $\Delta p = \|p_1 - p_2\|$ and $\nu_1 > 0 > \nu_2$ are the corresponding mSDF values. The orange triangle is extracted and the blue polygon is discarded.

²Inspiration drawn from the manga series *Ghost in the Shell*.

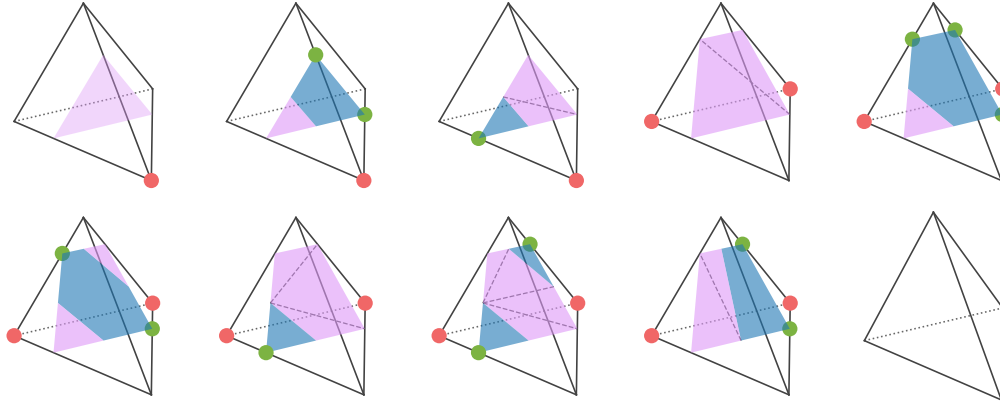


Figure 4: **G-SHELL** look-up table (up to rotational symmetry) for tetrahedral grids. Grid vertices with and without a red dot possess SDF values of opposite signs, and green dots on watertight mesh vertices indicates negative mSDF values. The pink regions represent the final extracted faces while the blue ones are the discarded regions on the watertight template mesh. Colored polygons other than triangles are cut along dashed lines.

Instead, we propose to jointly learn a general watertight mesh template, parameterized by a 3D grid of SDF values, in order to capture a larger set of meshes³. As we are not able to define ν with mesh topology changing over time, we instead define ν in the 3D space. Specifically, we store the discretized values of ν in a 3D grid. The mSDF value of any point in a grid cell can therefore be computed by a barycentric interpolation of the ν values on the grid cell vertices. We note that **G-SHELL** reduces to a typical watertight surface representation if all mSDF values on the grid are set to positive values (*i.e.*, no valid topological hole is defined on the manifold).

4.2 EFFICIENT MESH EXTRACTION WITH **G-SHELL**

With SDF and mSDF values stored in the same 3D grid, we obtain for **G-SHELL** an efficient Marching-Cubes-like algorithm which reuses the interpolation coefficient (*rf.* Eqn. 3) for the mSDF sign computation. Specifically, with an edge (p_i, p_j) , the corresponding SDF values $s_i < 0 < s_j$ and mSDF values ν_i, ν_j , we can compute the mSDF value on the extracted mesh vertex as $\nu' = (s_i\nu_j - s_j\nu_i)/(s_i - s_j)$. We give an example of the look-up table for tetrahedral grids in Figure 4, which enumerates all possible cases of SDF signs (on grid vertices) and mSDF signs (on watertight mesh vertices). Despite using tetrahedral grids as an example, we note that **G-SHELL** is generally applicable to other grid structures and not limited to tetrahedral grids.

5 APPLICATIONS OF **G-SHELL**

5.1 MESH RECONSTRUCTION FROM MULTIVIEW IMAGES

With **G-SHELL**, existing differentiable rasterization-based rendering methods (*e.g.*, [16, 41]) can be seamlessly applied for end-to-end reconstruction of both 3D watertight and non-watertight meshes from multiview RGB and binary mask images. Reconstruction with rasterization not only allows the final geometry to be explicitly optimized without pose-processing, but also saves memory and time compared to volumetric rendering with UDFs [34, 37] - there is no need to evaluate densities on a number of sample points per ray anymore. Moreover, with physics-based mesh rendering, one can jointly optimize geometry, material and lighting in a single stage.

We note, however, some particular difficulties in non-watertight mesh reconstruction from images. Unlike watertight meshes where we never get to see the inside surface, non-watertight surfaces have two sides and one side may be more visible than the other. For example, the inside of a long dress may not be fully observed and, when actually seen, it is also likely to be poorly illuminated. Similarly, indirect illumination has to be considered along with realistic materials (especially highly specular ones) and potentially complex geometry. To simplify the problem while still being able to demonstrate the effectiveness of the **G-SHELL** representation, we use an occlusion-aware differentiable renderer [16] that ignores indirect illumination but considers shadow rays.

³Indeed, any orientable open surface without self-intersection can be modeled thereby.

Another technical challenge is how to identify the existence and location of topological holes with only 2D images, particularly when only a limited number of views are available. We therefore propose to regularize the mSDF values of the reconstructed mesh by introducing a “hole-opening” loss (the mSDF is parameterized by a function with some parameter set θ_{mSDF}):

$$L_{\text{mSDF-reg}}(\theta_{\text{mSDF}}) = \underbrace{\sum_{u: \nu_{\theta_{\text{mSDF}}}(u) \geq 0} L_{\text{huber}}(\nu_{\theta_{\text{mSDF}}}(u)) + \tau \cdot \sum_{\substack{u': \nu_{\theta_{\text{mSDF}}}(u') = 0 \\ u' \text{ visible from some } q \in Q}} L_{\text{huber}}(\nu_{\theta_{\text{mSDF}}}(u') - \epsilon)}_{\text{Encourage hole opening}} \quad (1)$$

in which Q is the set of training camera poses, τ and ϵ are some positive scalars, L_{huber} is the Huber loss function. We introduce the second regularization term to discourage topological holes from being too large, especially during the early stage of the optimization process. We provide all the details regarding the remaining regularization losses and other training settings in Appendix B.

5.2 G-MESHDIFFUSION: GENERATIVE MODELING OF GEOMETRY

With the regular grid structure of the **G-SHELL** parameterization, it is straightforward to train generative models to produce the grid attributes (SDF, mSDF and potentially grid deformation) to enable non-watertight mesh generation. Indeed, **G-SHELL** enables generative modeling with diffusion models [18] in which a regular input structure is necessary.

To demonstrate the generative modeling of **G-SHELL**, we consider MeshDiffusion [35], which generates watertight meshes by sampling SDF and grid deformation in a 3D tetrahedral grid, to generate non-watertight meshes. Although it is possible to simply introduce the additional dimension of mSDF on the grid vertex attributes, the generated shapes can be noisy as pointed out in [35]. Specifically, the boundary vertices of a generated non-watertight mesh are computed via an interpolation with mSDF:

$$u' = \frac{|\nu_1|}{|\nu_1 - \nu_2|} \cdot u_2 - \frac{|\nu_2|}{|\nu_1 - \nu_2|} \cdot u_1, \quad \nu_1 < 0 < \nu_2, \quad (2)$$

in which (u_1, u_2) is an edge on the extracted watertight template and ν_1, ν_2 are the corresponding mSDF values. Because ν_i can be any real number, a naïve diffusion loss results in unevenly weighted prediction on u' . One could normalize ν to ± 1 , similar to what MeshDiffusion does for the SDF values, but it comes at the cost of expressiveness as the grid deformation is already used to compensate the error resulting from the normalization of SDF values.

We therefore propose a modified version of the MeshDiffusion architecture to generate continuous mSDF values. Specifically, by setting $\alpha = |\nu_1|/|\nu_1 - \nu_2|$, we rewrite Eqn. 2 into a linear mapping of (u_1, u_2) : $u' = \alpha u_2 - (1 - \alpha)u_1$. As a result, we may alternatively generate the linear interpolation coefficient α , which is bounded in $[0, 1]$. In the case of tetrahedral grids as in DMTet, there are 12 candidate edges (u_i, u_j) in each single cell since u_i 's always lie on tetrahedral grid edges. We simply set the diffusion model to generate all α 's for these candidates edges in each single cell. The α 's to be used are eventually chosen based on the configuration of each generated tetrahedral cell (as in Figure 4). Similar to MeshDiffusion, we collect a dataset of non-watertight meshes by running inverse rendering on multiview datasets of 3D objects. We term our final diffusion model on the **G-SHELL** representation as *G-MeshDiffusion*. More details can be found in Appendix C.

6 EXPERIMENTS AND RESULTS

6.1 RECONSTRUCTION FROM MULTIVIEW IMAGES

Baselines. We compare our method to current state-of-the-art methods for non-watertight mesh reconstruction: NeuralUDF [37], NeUDF [34] and NeAT [39]. We also evaluate watertight reconstruction methods including NeuS [55] and Nvdiffrmc [16] (with DMTet [50]). We follow the original settings of these baselines, but train them for 400,000 iterations with mask loss weighted by 0.1. During testing, the novel views are rendered and subsequently evaluated at a resolution of 512. For UDF-based methods, the non-watertight explicit meshes are extracted using MeshUDF [14], while for SDF-based methods (NeuS/NeAT), the meshes are extracted with Marching Cubes [38] with the same resolution. For Nvdiffrmc with DMTet, we use a grid resolution of 128.

Dataset. We use DeepFashion3D-v2 [17] to quantitatively evaluate the performance of reconstruction with **G-SHELL** on non-watertight meshes. Specifically, we use ground truth meshes of 9 instances

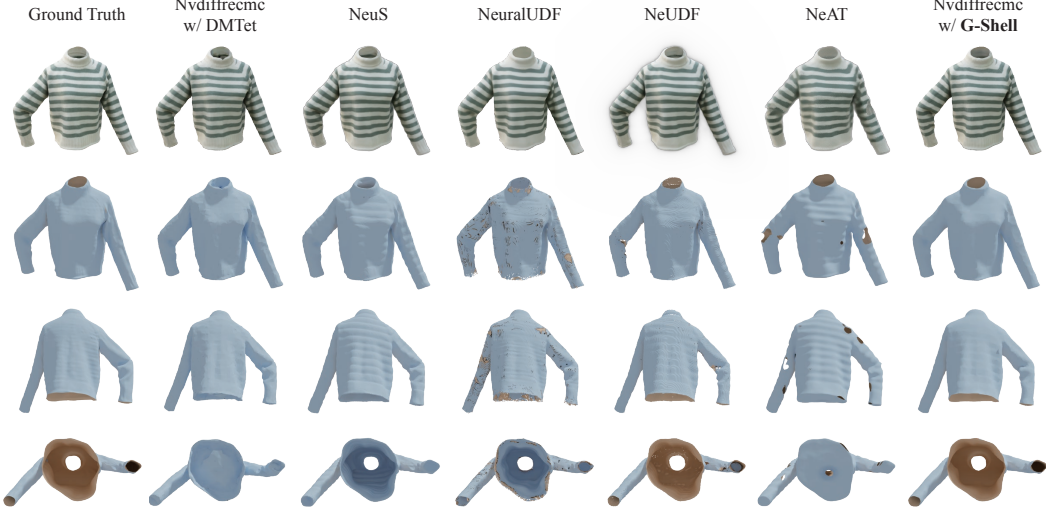


Figure 5: Comparison between reconstruction w/ **G-SHELL** and other baseline methods on multiview reconstruction on DeepFashion3D dataset. Top row: reconstructed texture. Bottom 3 rows: reconstructed meshes.

Method \ Instance ID	30	92	117	133	164	320	448	522	591	Avg
NeuS [55]	31.876	26.850	29.234	29.692	30.405	33.827	31.591	32.846	26.282	30.289
Nvdiffrecmc w/ DMTet [50]	32.570	33.542	28.143	30.814	28.781	32.336	33.917	32.144	32.872	31.677
NeuralUDF [37]	30.264	25.887	28.908	31.115	28.463	30.739	32.185	29.965	32.574	30.011
NeUDF [34]	30.312	31.957	27.448	30.275	28.324	32.568	32.511	31.371	<u>34.898</u>	31.074
NeAT [39]	27.407	28.228	24.129	26.944	24.887	29.630	30.846	27.149	29.841	27.674
Nvdiffrecmc w/ G-SHELL	<u>33.165</u>	<u>33.959</u>	30.204	<u>33.164</u>	<u>31.139</u>	33.429	34.997	<u>32.724</u>	34.579	<u>33.039</u>
Nvdiffrecmc w/ G-SHELL (FC)	33.169	34.615	<u>30.223</u>	33.368	31.735	<u>33.611</u>	<u>34.897</u>	32.499	35.427	33.277

Table 1: PSNR (\uparrow) on DeepFashion3D garment instances. Marker: **1st rank** and 2nd rank.

from DeepFashion3D-v2 that overlap with the instances of DeepFashion3D-v1 used in [34, 37]. Different from previous work, such as NeuralUDF, that uses albedo images for training and testing, we instead use images rendered with realistic lighting and shading. Specifically, for each instance we use Blender with Cycles engine and realistic environment lightmap to render 72 views (RGB images and binary segmentation masks) for training and 200 views for testing.

Settings. For the multi-view reconstruction with **G-SHELL**, we set the grid resolution to 128 for tetrahedral grids and 80 for FlexiCubes, and train the models with 5000 iterations using a batch size of 2 views. For all baseline methods, we use the default settings as in their papers. Our experiments are carried out with tetrahedral grid implementation of **G-SHELL** by default, if not otherwise specified. To demonstrate that the idea of **G-SHELL** can be quite general, we also evaluate a simple variant of **G-SHELL** implemented with FlexiCubes [51], denoted by **G-SHELL** (FC) in Table 1 and Table 2.

Reconstruction quality. Table 1 shows the PSNR averaged over all test views. For all shapes fitted with implicit-based baseline methods (*i.e.*, except for Nvdiffrecmc with DMTet), we render images directly from the learned implicit fields instead of the extracted meshes. We also evaluate all methods on the quality of the reconstructed geometry by computing the bi-directional pointcloud-to-mesh Chamfer distance. The results are given in Table 2, from which we see that **G-SHELL** achieves excellent reconstruction quality and outperforms a number of state-of-the-art methods. Figure 5 gives a qualitative comparison, where the front and back mesh faces (re-oriented to be consistent to their neighbors) are painted in different colors. The qualitative results in Figure 6 demonstrates that the mesh topology reconstructed by **G-SHELL** with FlexiCubes is more regular than **G-SHELL** with tetrahedral grids, making it better suited for physical simulation. More results are in Appendix D.

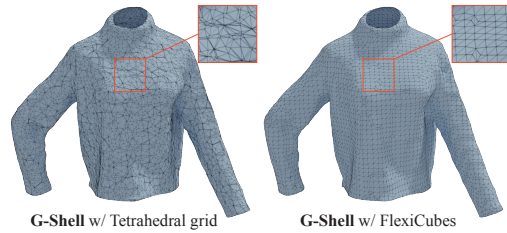


Figure 6: Reconstructed mesh topology of **G-SHELL** with tetrahedral grids and **G-SHELL** with FlexiCubes. Mesh vertex count: Left = 10,658, Right = 6,183.

Method \ Instance ID	30	92	117	133	164	320	448	522	591	Avg
NeuS [55]	0.450	1.244	0.505	0.709	0.528	0.426	0.734	0.598	1.737	0.770
Nvdiffraycast w/ DMTet [50]	0.629	0.466	0.724	0.856	0.722	0.444	0.444	0.649	1.026	0.662
NeuralUDF [37]	0.457	0.867	0.281	0.215	0.198	0.554	0.197	0.561	0.206	0.393
NeUDF [34]	0.315	0.458	0.204	0.107	0.184	0.432	0.159	0.585	0.128	0.286
NeAT [39]	0.605	0.325	1.010	0.873	0.538	0.305	0.323	0.591	0.237	0.534
Nvdiffraycast w/ G-SHELL	0.212	0.207	0.133	<u>0.144</u>	<u>0.160</u>	0.173	<u>0.173</u>	0.208	<u>0.178</u>	0.177
Nvdiffraycast (FC)	<u>0.235</u>	<u>0.227</u>	<u>0.146</u>	0.154	0.165	<u>0.229</u>	0.195	<u>0.261</u>	0.234	<u>0.203</u>

Table 2: **Chamfer distance (cm ↓)** on DeepFashion3D garment instances. Marker: **1st rank** and **2nd rank**.

Method \ Metalness	0	0.2	0.4	0.6	0.8	1	Avg	Method \ Metalness	0	0.2	0.4	0.6	0.8	1	Avg
NeuS [55]	33.59	32.03	31.62	31.21	30.58	30.45	31.58	NeuS [55]	0.47	0.59	0.50	0.57	0.68	0.72	0.59
NeuralUDF [37]	31.42	29.54	29.45	29.39	29.25	28.98	29.67	NeuralUDF [37]	0.51	1.06	1.05	0.98	0.53	0.85	0.83
NeUDF [34]	32.45	29.32	29.04	29.19	29.13	29.18	29.72	NeUDF [34]	0.26	0.52	0.40	0.45	0.70	0.44	0.46
NeAT [39]	28.41	27.37	28.07	26.93	26.58	26.85	27.37	NeAT [39]	0.59	0.65	0.61	0.68	0.70	0.73	0.66
G-SHELL	36.01	34.23	32.86	33.08	32.93	32.31	33.57	G-SHELL	0.20	0.22	0.28	0.24	0.24	0.27	0.24

Table 3: Ablation study on metallic materials. We use Nvdiffraycast along with the proposed **G-SHELL** for our reconstruction in the experiment. Left: **PSNR (↑)**. Right: **Chamfer distance (cm ↓)**.

From Figure 5, we can observe that our method achieves much better prediction on novel views than the other baselines due to the better modeling of lighting, occlusion and material. Due to the highly concave structure in the clothing interior, we can also see that watertight reconstruction baselines often fail to reconstruct the inner side of clothing in the DeepFashion3D dataset.

Efficiency in training and inference. In addition, we compare the runtime of all non-watertight methods (tested on the same machine with a single NVIDIA RTX 6000 GPU). Along with Nvdiffraycast, **G-SHELL** takes only **3 hours** to fit a ground truth shape while NeuralUDF, NeUDF and NeAT take 17.3, 16.4, and 4.3 hours, respectively. For novel-view synthesis with all images rendered with a resolution of 512×512 , our method runs at **2.7 sec/img** (inferring from a learned tetrahedral grid with the Nvdiffrast rasterizer [26]), while NeuralUDF, NeUDF and NeAT run at 1.8 min/img, 1.4 min/img, and 9.7 min/img, respectively. Compared to the other methods, ours is significantly faster in both training and inference due to its highly efficient rasterization.

6.2 HYBRID WATERTIGHT AND NON-WATERTIGHT MESH RECONSTRUCTION

To demonstrate that **G-SHELL** is capable of reconstructing both watertight and non-watertight shapes at the same time, we test our method on an instance from the synthetic NeRF dataset [40] in which all the images are taken from the objects above and never below. We adopt a minimalist assumption that the unseen regions should always be empty and reconstruct the target shapes with the **G-SHELL** representation. On the left hand side of Figure 7, we show that the upper surface of the target shape are well reconstructed without adding any unnecessary lower surface faces. On the right hand side of Figure 7, we also visualize the generalized winding number [2, 20], a metric that is capable of quantifying local manifoldness. The result demonstrates that **G-SHELL** is able to reconstruct a hybrid shape that involves both watertight and non-watertight meshes where the unobserved regions tend to be reconstructed as single-layered surfaces without introducing additional meshes.

6.3 RECONSTRUCTION UNDER SPECULAR LIGHTING

One key advantage of mesh inverse rendering is that geometries may be reconstructed in cases of complex lighting and materials. To demonstrate such an advantage, we conduct ablation experiments and compare the performance of non-watertight mesh reconstruction methods on shapes with specular surfaces. Specifically, we modify the material of the sweater mesh presented in Figure 5 by setting the roughness parameter to 0.4 and create a set of meshes with the metalness parameter ranging from 0 to 1. We use the same set of hyperparameters for the experiment. Results in Table 1 and Table 3 verify that **G-SHELL** can well reconstruct both images and shapes under complex lighting and materials.



Figure 7: Left: the reconstructed mesh, with back faces painted orange. Right: winding number visualization; regions colored red are locally more manifold-like.

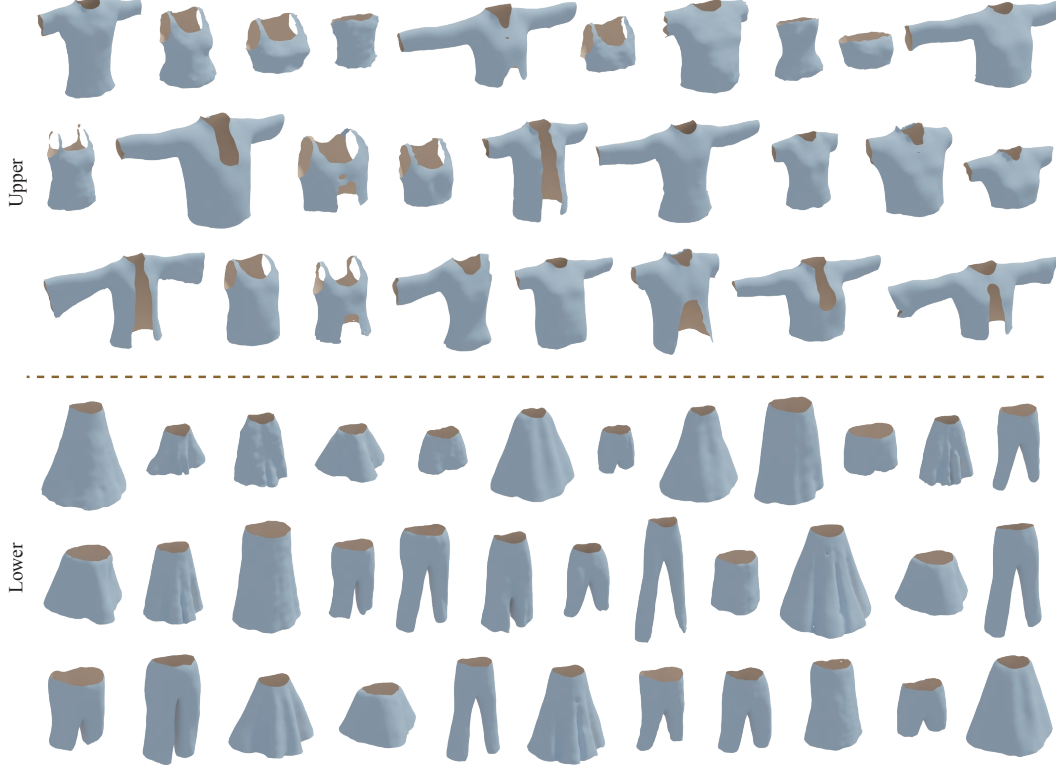


Figure 8: Samples of unconditionally generated upper and lower outfits by G-MeshDiffusion.

Method	MMD (10^{-3} , ↓)		COV (% , ↑)		1-NNA (% , ↓)		MV-FID (↓)	
	CD	EMD	CD	EMD	CD	EMD		
Lower Garments	MeshDiffusion [35]	1.88	68.72	38.01	31.79	88.99	91.03	191.09
	GET3D [11]	1.57	57.19	46.00	48.13	79.66	72.82	95.69
	G-MeshDiffusion	1.36	55.30	41.92	41.03	68.29	67.23	79.01
Upper Garments	MeshDiffusion [35]	1.24	55.37	51.51	46.71	77.44	78.77	167.69
	GET3D [11]	1.37	56.86	48.85	43.87	84.37	80.11	112.45
	G-MeshDiffusion	1.05	51.15	51.33	49.20	61.37	60.66	88.98

Table 4: Quantitative results of the proposed **G-SHELL** diffusion model (G-MeshDiffusion).

6.4 GENERATIVE 3D MESH MODELING

Baselines. As there are no mesh generative models for open surfaces with manifold structures, we compare our method with two watertight mesh generative models: MeshDiffusion [35] and GET3D [11], both using the SDF-based DMTet [50] as the representation. Detailed training settings are deferred to Appendix C. We implement **G-SHELL** with tetrahedral grids in this experiment.

Dataset. We collect meshes in 4 categories (T-shirt, Top, Skirts, Trousers) from the Cloth3D dataset [4] and regroup them into two new categories: upper garments (including T-shirt and Top) and lower garments (including Skirts and Trousers). For both MeshDiffusion (using the DMTet representation) G-MeshDiffusion (using the **G-SHELL** representation), we run inverse rendering on meshes with known environment lightmaps and known materials using RGB, binary mask, and depth supervision. We generally follow the same settings of [35] for G-MeshDiffusion. For GET3D, we follow the same training setting as [11] and render multiview RGB images for training.

Evaluation metrics. For each model, we sample a set of meshes, with the size of the test sets, using 100 steps of DDIM [52] and apply standard Laplacian smoothing to these meshes. Similar to [11, 35], we evaluate point cloud metrics between the point clouds sampled from generated meshes and those from ground truth meshes. To compensate the lack of perceptual measure in the point cloud metrics, we also evaluate the generated results with multiview FID (MV-FID) [35, 63], which is computed by an average of FID (Fréchet Inception Distance) scores of 20 views (rendered with fixed light sources

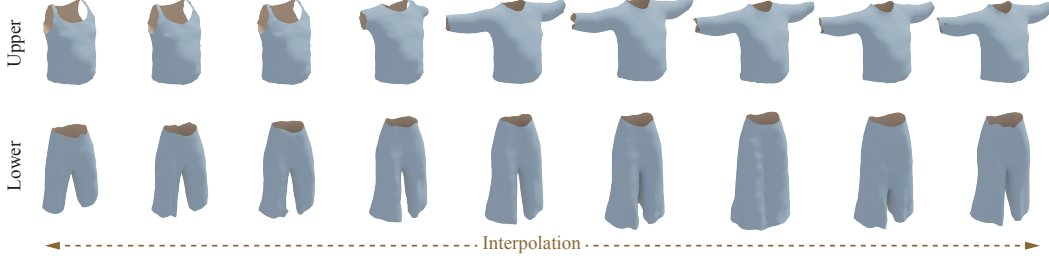


Figure 9: Interpolation results of our generated samples.

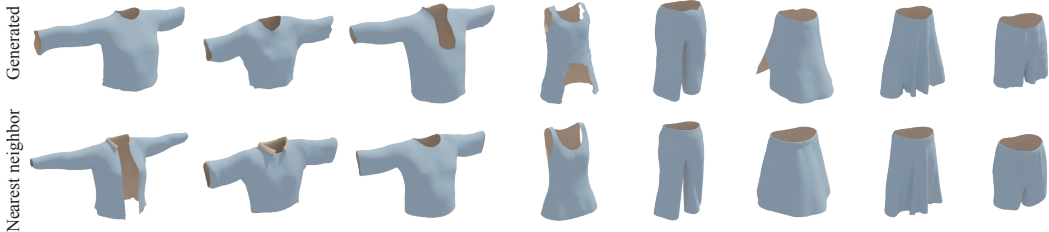


Figure 10: Nearest neighbor of our generated sample in the training set.

and a diffuse-only mesh material). During rendering, we do not re-orient the face normals towards the camera so that the difference between watertight and open surfaces can be taken into account.

Qualitative and quantitative results. The quantitative results are given in Table 4. We observe that G-MeshDiffusion generally achieves better performance than the watertight mesh generation methods (MeshDiffusion and GET3D), but more importantly, G-MeshDiffusion can better capture the single-sided nature of non-watertight meshes as it achieves a significantly better MV-FID score. In addition, we qualitatively show some unconditionally sampled meshes from G-MeshDiffusion in Figure 8. Following [35], we also provide some interpolation sequences (obtained by spherical linear interpolation with the initial Gaussian noises using 100-step DDIM inference) in Figure 9. The interpolation results demonstrate a smooth transition across different clothing styles. Finally, we show in Figure 10 the nearest neighbor of our generated meshes in the training set. The results show that G-MeshDiffusion does not memorize the training samples and can generate novel shapes.

7 DISCUSSION ON LIMITATIONS

Representation. **G-SHELL** is not able to model shapes with self-intersections. Nor does it model non-orientable surfaces such as Möbius strips, since the use of SDF implies orientability. Besides, compared to implicit-based methods of which the resolution can be viewed as “infinite”, **G-SHELL** generally may require a higher resolution in order to model tiny topological holes.

Mesh reconstruction. The discontinuity in mesh rendering poses a severe optimization problem when the target geometry is complex, since the entanglement between geometry and indirect illumination comes into play. In this paper, we only take shadow rays into consideration, but in more complex scenarios one might need to model indirect illumination.

Mesh generation. 3D U-Nets are not memory-efficient, and it is hard to scale them to high resolutions. Future work for better generative modeling with **G-SHELL** may include more efficient architectures such as those using triplane features [6], and alternative 3D generative methods similar to GET3D [11].

8 CONCLUDING REMARKS

Our proposed **G-SHELL** is a general 3D mesh representation which models both watertight and non-watertight meshes. By introducing the new quantity of manifold signed distance field (mSDF) on a learnable watertight mesh template with varying topology, we enable both rasterization-based reconstruction and diffusion-model-based unconditional generation of non-watertight meshes. Such a design lead to better performance and greater flexibility in non-watertight mesh modeling. Still, **G-SHELL** is only able to parameterize a limited subset of meshes, especially when limited computational resources are available. Furthermore, it calls for better inverse rendering and generative modeling techniques to fully leverage the flexibility of **G-SHELL**.

ACKNOWLEDGEMENT

We sincerely thank Peter Kulits for paper proofreading and Zhouyingcheng Liao for creating physical simulation demos. Authors listed as equal contribution (*resp.*, shared last author) are allowed to switch their orders in the author list in their resumes and websites. The paper title was proposed during an after-dinner coffee chat among Zhen Liu, Yao Feng, Yuliang Xiu, Weiyang Liu and Tim Xiao, especially due to Yuliang Xiu (for proposing "Shell") and Weiyang Liu (for the connection to the manga series *Ghost in the Shell*⁴).

Disclosure. This work was supported by the German Federal Ministry of Education and Research (BMBF): Tübingen AI Center, FKZ: 01IS18039B, and by the Machine Learning Cluster of Excellence, EXC number 2064/1 – Project number 390727645. MJB has received research gift funds from Adobe, Intel, Nvidia, Meta/Facebook, and Amazon. MJB has financial interests in Amazon, Datalog Technologies, and Meshcapade GmbH. While MJB is a part-time employee of Meshcapade, his research was performed solely at, and funded solely by, the Max Planck Society. LP is supported by the Canada CIFAR AI Chairs Program and NSERC Discovery Grant. WL was supported by the German Research Foundation (DFG): SFB 1233, Robust Vision: Inference Principles and Neural Mechanisms, TP XX, project number: 276693517. YF is partially supported by the Max Planck ETH Center for Learning Systems. YX is funded by the European Union's Horizon 2020 research and innovation programme under the Marie Skłodowska-Curie grant agreement No.860768 (CLIQUE).

REFERENCES

- [1] L.V. Ahlfors and L. Sario. *Riemann Surfaces: (PMS-26)*. Princeton Mathematical Series. Princeton University Press, 2015.
- [2] Gavin Barill, Neil G Dickson, Ryan Schmidt, David IW Levin, and Alec Jacobson. Fast winding numbers for soups and clouds. *ACM Transactions on Graphics*, 37(4):1–12, 2018.
- [3] Fausto Bernardini, Joshua Mittleman, Holly Rushmeier, Cláudio Silva, and Gabriel Taubin. The ball-pivoting algorithm for surface reconstruction. *IEEE transactions on visualization and computer graphics*, 5(4):349–359, 1999.
- [4] Hugo Bertiche, Meysam Madadi, and Sergio Escalera. Cloth3d: clothed 3d humans. In *ECCV*, 2020.
- [5] Mario Botsch and Leif Kobbelt. A remeshing approach to multiresolution modeling. In *Eurographics*, 2004.
- [6] Eric R Chan, Connor Z Lin, Matthew A Chan, Koki Nagano, Boxiao Pan, Shalini De Mello, Orazio Gallo, Leonidas J Guibas, Jonathan Tremblay, Sameh Khamis, et al. Efficient geometry-aware 3d generative adversarial networks. In *CVPR*, 2022.
- [7] Eric R Chan, Marco Monteiro, Petr Kellnhofer, Jiajun Wu, and Gordon Wetzstein. pi-gan: Periodic implicit generative adversarial networks for 3d-aware image synthesis. In *CVPR*, 2021.
- [8] Rui Chen, Yongwei Chen, Ningxin Jiao, and Kui Jia. Fantasia3d: Disentangling geometry and appearance for high-quality text-to-3d content creation. In *ICCV*, 2023.
- [9] Zhiqin Chen, Andrea Tagliasacchi, Thomas Funkhouser, and Hao Zhang. Neural dual contouring. *ACM Transactions on Graphics*, 41(4), 2022.
- [10] Julian Chibane, Gerard Pons-Moll, et al. Neural unsigned distance fields for implicit function learning. In *NeurIPS*, 2020.
- [11] Jun Gao, Tianchang Shen, Zian Wang, Wenzheng Chen, Kangxue Yin, Daiqing Li, Or Litany, Zan Gojcic, and Sanja Fidler. Get3d: A generative model of high quality 3d textured shapes learned from images. In *NeurIPS*, 2022.
- [12] William Gao, April Wang, Gal Metzer, Raymond A Yeh, and Rana Hanocka. Tetgan: A convolutional neural network for tetrahedral mesh generation. In *BMVC*, 2022.
- [13] Amos Gropp, Lior Yariv, Niv Haim, Matan Atzmon, and Yaron Lipman. Implicit geometric regularization for learning shapes. In *ICML*, 2020.

⁴https://en.wikipedia.org/wiki/Ghost_in_the_Shell

- [14] Benoit Guillard, Federico Stella, and Pascal Fua. Meshudf: Fast and differentiable meshing of unsigned distance field networks. In *ECCV*, 2022.
- [15] Rana Hanocka, Gal Metzger, Raja Giryes, and Daniel Cohen-Or. Point2mesh: A self-prior for deformable meshes. *ACM Trans. Graph.*, 39(4), 2020.
- [16] Jon Hasselgren, Nikolai Hofmann, and Jacob Munkberg. Shape, Light, and Material Decomposition from Images using Monte Carlo Rendering and Denoising. In *NeurIPS*, 2022.
- [17] Zhu Heming, Cao Yu, Jin Hang, Chen Weikai, Du Dong, Wang Zhangye, Cui Shuguang, and Han Xiaoguang. Deep fashion3d: A dataset and benchmark for 3d garment reconstruction from single images. In *ECCV*, 2020.
- [18] Jonathan Ho, Ajay Jain, and Pieter Abbeel. Denoising diffusion probabilistic models. In *NeurIPS*, 2020.
- [19] Jingwei Huang, Hao Su, and Leonidas Guibas. Robust watertight manifold surface generation method for shapenet models. *arXiv preprint arXiv:1802.01698*, 2018.
- [20] Alec Jacobson, Ladislav Kavan, and Olga Sorkine-Hornung. Robust inside-outside segmentation using generalized winding numbers. *ACM Transactions on Graphics*, 32(4):1–12, 2013.
- [21] Yue Jiang, Dantong Ji, Zhizhong Han, and Matthias Zwicker. Sdfdiff: Differentiable rendering of signed distance fields for 3d shape optimization. In *CVPR*, 2020.
- [22] Tao Ju, Frank Losasso, Scott Schaefer, and Joe Warren. Dual contouring of hermite data. In *SIGGRAPH*, 2002.
- [23] Michael Kazhdan, Matthew Bolitho, and Hugues Hoppe. Poisson surface reconstruction. In *SGP*, 2006.
- [24] Bernhard Kerbl, Georgios Kopanas, Thomas Leimkühler, and George Drettakis. 3d gaussian splatting for real-time radiance field rendering. *ACM Transactions on Graphics*, 42(4):1–14, 2023.
- [25] Adam R Kosiorek, Heiko Strathmann, Daniel Zoran, Pol Moreno, Rosalia Schneider, Sona Mokrá, and Danilo Jimenez Rezende. Nerf-vae: A geometry aware 3d scene generative model. In *ICML*, 2021.
- [26] Samuli Laine, Janne Hellsten, Tero Karras, Yeongho Seol, Jaakko Lehtinen, and Timo Aila. Modular primitives for high-performance differentiable rendering. *ACM Transactions on Graphics*, 39(6):1–14, 2020.
- [27] Der-Tsai Lee and Bruce J Schachter. Two algorithms for constructing a delaunay triangulation. *International Journal of Computer & Information Sciences*, 9(3):219–242, 1980.
- [28] J. Lee. *Introduction to Topological Manifolds*. Graduate Texts in Mathematics. Springer New York, 2010.
- [29] Yiyi Liao, Simon Donne, and Andreas Geiger. Deep marching cubes: Learning explicit surface representations. In *CVPR*, 2018.
- [30] Chen-Hsuan Lin, Jun Gao, Luming Tang, Towaki Takikawa, Xiaohui Zeng, Xun Huang, Karsten Kreis, Sanja Fidler, Ming-Yu Liu, and Tsung-Yi Lin. Magic3d: High-resolution text-to-3d content creation. In *CVPR*, 2023.
- [31] Shaohui Liu, Yinda Zhang, Songyou Peng, Boxin Shi, Marc Pollefeys, and Zhaopeng Cui. Dist: Rendering deep implicit signed distance function with differentiable sphere tracing. In *CVPR*, 2020.
- [32] Shichen Liu, Shunsuke Saito, Weikai Chen, and Hao Li. Learning to infer implicit surfaces without 3d supervision. In *NeurIPS*, 2019.
- [33] Weiyang Liu, Zhen Liu, Liam Paull, Adrian Weller, and Bernhard Schölkopf. Structural causal 3d reconstruction. In *ECCV*, 2022.
- [34] Yu-Tao Liu, Li Wang, Jie Yang, Weikai Chen, Xiaoxu Meng, Bo Yang, and Lin Gao. Neudf: Leaning neural unsigned distance fields with volume rendering. In *CVPR*, 2023.
- [35] Zhen Liu, Yao Feng, Michael J. Black, Derek Nowrouzezahrai, Liam Paull, and Weiyang Liu. Meshdiffusion: Score-based generative 3d mesh modeling. In *ICLR*, 2023.
- [36] Stephen Lombardi, Tomas Simon, Jason Saragih, Gabriel Schwartz, Andreas Lehrmann, and Yaser Sheikh. Neural volumes: learning dynamic renderable volumes from images. *ACM Transactions on Graphics*, 38(4):1–14, 2019.

- [37] Xiaoxiao Long, Cheng Lin, Lingjie Liu, Yuan Liu, Peng Wang, Christian Theobalt, Taku Komura, and Wenping Wang. Neuraludf: Learning unsigned distance fields for multi-view reconstruction of surfaces with arbitrary topologies. In *CVPR*, 2023.
- [38] William E Lorensen and Harvey E Cline. Marching cubes: A high resolution 3d surface construction algorithm. In *SIGGRAPH*, 1987.
- [39] Xiaoxu Meng, Weikai Chen, and Bo Yang. Neat: Learning neural implicit surfaces with arbitrary topologies from multi-view images. In *CVPR*, 2023.
- [40] Ben Mildenhall, Pratul P Srinivasan, Matthew Tancik, Jonathan T Barron, Ravi Ramamoorthi, and Ren Ng. Nerf: Representing scenes as neural radiance fields for view synthesis. In *ECCV*, 2020.
- [41] Jacob Munkberg, Jon Hasselgren, Tianchang Shen, Jun Gao, Wenzheng Chen, Alex Evans, Thomas Mueller, and Sanja Fidler. Extracting Triangular 3D Models, Materials, and Lighting From Images. In *CVPR*, 2022.
- [42] Charlie Nash, Yaroslav Ganin, SM Ali Eslami, and Peter Battaglia. Polygen: An autoregressive generative model of 3d meshes. In *ICML*, 2020.
- [43] Junyi Pan, Xiaoguang Han, Weikai Chen, Jiapeng Tang, and Kui Jia. Deep mesh reconstruction from single rgb images via topology modification networks. In *ICCV*, 2019.
- [44] Songyou Peng, Chiyu Jiang, Yiyi Liao, Michael Niemeyer, Marc Pollefeys, and Andreas Geiger. Shape as points: A differentiable poisson solver. In *NeurIPS*, 2021.
- [45] Lingteng Qiu, Guanying Chen, Jiapeng Zhou, Mutian Xu, Junle Wang, and Xiaoguang Han. Rec-mv: Reconstructing 3d dynamic cloth from monocular videos. In *CVPR*, 2023.
- [46] Edoardo Remelli, Artem Lukoianov, Stephan Richter, Benoit Guillard, Timur Bagautdinov, Pierre Baque, and Pascal Fua. Meshsdf: Differentiable iso-surface extraction. In *NeurIPS*, 2020.
- [47] Ian Richards. On the classification of noncompact surfaces. *Transactions of the American Mathematical Society*, 106(2):259–269, 1963.
- [48] Katja Schwarz, Yiyi Liao, Michael Niemeyer, and Andreas Geiger. Graf: Generative radiance fields for 3d-aware image synthesis. In *NeurIPS*, 2020.
- [49] Silvia Sellán and Alec Jacobson. Stochastic poisson surface reconstruction. *ACM Transactions on Graphics*, 2022.
- [50] Tianchang Shen, Jun Gao, Kangxue Yin, Ming-Yu Liu, and Sanja Fidler. Deep marching tetrahedra: a hybrid representation for high-resolution 3d shape synthesis. In *NeurIPS*, 2021.
- [51] Tianchang Shen, Jacob Munkberg, Jon Hasselgren, Kangxue Yin, Zian Wang, Wenzheng Chen, Zan Gojcic, Sanja Fidler, Nicholas Sharp, and Jun Gao. Flexible isosurface extraction for gradient-based mesh optimization. *ACM Transactions on Graphics*, 42(4):1–16, 2023.
- [52] Jiaming Song, Chenlin Meng, and Stefano Ermon. Denoising diffusion implicit models. In *ICLR*, 2020.
- [53] Graham M Treece, Richard W Prager, and Andrew H Gee. Regularised marching tetrahedra: improved iso-surface extraction. *Computers & Graphics*, 23(4):583–598, 1999.
- [54] Nanyang Wang, Yinda Zhang, Zhuwen Li, Yanwei Fu, Wei Liu, and Yu-Gang Jiang. Pixel2mesh: Generating 3d mesh models from single rgb images. In *ECCV*, 2018.
- [55] Peng Wang, Lingjie Liu, Yuan Liu, Christian Theobalt, Taku Komura, and Wenping Wang. Neus: Learning neural implicit surfaces by volume rendering for multi-view reconstruction. *NeurIPS*, 2021.
- [56] Xingkui Wei, Zhengqing Chen, Yanwei Fu, Zhaopeng Cui, and Yinda Zhang. Deep hybrid self-prior for full 3d mesh generation. In *ICCV*, 2021.
- [57] Jiajun Wu, Chengkai Zhang, Tianfan Xue, Bill Freeman, and Josh Tenenbaum. Learning a probabilistic latent space of object shapes via 3d generative-adversarial modeling. In *NIPS*, 2016.
- [58] Yuliang Xiu, Jinlong Yang, Xu Cao, Dimitrios Tzionas, and Michael J. Black. ECON: Explicit Clothed humans Optimized via Normal integration. In *Proceedings of the IEEE/CVF Conference on Computer Vision and Pattern Recognition (CVPR)*, June 2023.

- [59] Yuxuan Xue, Bharat Lal Bhatnagar, Riccardo Marin, Nikolaos Sarafianos, Yuanlu Xu, Gerard Pons-Moll, and Tony Tung. Nsf: Neural surface fields for human modeling from monocular depth. In *ICCV*, 2023.
- [60] Guandao Yang, Xun Huang, Zekun Hao, Ming-Yu Liu, Serge Belongie, and Bharath Hariharan. Pointflow: 3d point cloud generation with continuous normalizing flows. In *ICCV*, 2019.
- [61] Lior Yariv, Yoni Kasten, Dror Moran, Meirav Galun, Matan Atzmon, Basri Ronen, and Yaron Lipman. Multiview neural surface reconstruction by disentangling geometry and appearance. In *NeurIPS*, 2020.
- [62] Xiaohui Zeng, Arash Vahdat, Francis Williams, Zan Gojcic, Or Litany, Sanja Fidler, and Karsten Kreis. Lion: Latent point diffusion models for 3d shape generation. In *NeurIPS*, 2022.
- [63] Xin-Yang Zheng, Yang Liu, Peng-Shuai Wang, and Xin Tong. Sdf-stylegan: Implicit sdf-based stylegan for 3d shape generation. In *SGP*, 2022.
- [64] Heming Zhu, Lingteng Qiu, Yuda Qiu, and Xiaoguang Han. Registering explicit to implicit: Towards high-fidelity garment mesh reconstruction from single images. In *CVPR*, 2022.

Appendix

Table of Contents

A Some Mathematics on Surfaces	16
B Detailed Settings on Mesh Reconstruction	17
B.1 Losses	17
B.2 Differences in implementations for lighting regularization	19
B.3 Rendering, optimization and other settings	19
C Detailed Settings on Diffusion Models with G-SHELL	20
C.1 Grid storage of interpolation coefficients from mSDF	20
C.2 Architecture and training settings	20
C.3 Data preparation	20
D More Qualitative Examples of Multi-view Mesh Reconstruction	21
E Reconstructed Meshes for Surfaces with Complex Patterns	24
F Reconstruction of Shapes with Metallic Materials	25
G On mSDF Regularization	26

A SOME MATHEMATICS ON SURFACES

We first state the condition for homeomorphism between compact triangulable bordered surfaces⁵:

Theorem 1 ([47]) *Two compact triangulable bordered surfaces are homeomorphic if and only if they both have the same number of boundary curves, the same Euler characteristic, and are either both orientable or else both non-orientable.*

It is apparent that any simply-connected surface is homeomorphic to a compact disk on a sphere, since simply-connected bordered surfaces are triangulable.

Indeed, one may establish a more general relation between compact bordered surfaces and closed surfaces with the following classification theorem:

Theorem 2 (Classification Theorem of Surfaces [28]) *Every compact surface (without boundary) is homeomorphic to one of the following:*

- *The sphere \mathbb{S} .*
- *A connected sum of tori: $\mathbb{T} \# \dots \# \mathbb{T}$.*
- *A connected sum of projective planes: $\mathbb{P}^2 \# \dots \# \mathbb{P}^2$*

Together with Theorem 1, one may conclude that any connected orientable bordered surface (which is triangulable) is homeomorphic to a compact bordered surface on either a sphere or a connected sum of tori.

We conclude this section by noting the following theorem:

Theorem 3 ([1]) *Every bordered surface $\overline{\mathcal{F}}$ can be regularly embedded in a surface. If $\overline{\mathcal{F}}$ is compact, it can be regularly embedded in a closed surface.*

⁵i.e., 2-manifolds, as opposed to the casual daily-life definition of surfaces.

B DETAILED SETTINGS ON MESH RECONSTRUCTION

B.1 LOSSES

RGB and mask supervision. Given multiview RGB images I_{GT} and the corresponding binary masks M_{GT} (to segment foreground from background), we optimize the following losses:

$$L_{\text{RGB}} = \|I_{\text{RGB, Rendered}} - I_{\text{RGB, GT}}\|_2^2, \quad (3)$$

$$L_{\text{mask}} = \|M_{\text{Rendered}} - M_{\text{GT}}\|_2^2. \quad (4)$$

Since the direct output of the renderer is a high-dynamic range (HDR) image $\hat{I}_{\text{RGB, Rendered}}$, we follow [16] and use the same tonemapper Γ to map the HDR image into a sRGB image with pixels in the range $[0, 255]$:

$$I_{\text{RGB, Rendered}} = T(\hat{I}_{\text{RGB, Rendered}}) = \Gamma(\log(\hat{I}_{\text{RGB, Rendered}} + 1)), \quad (5)$$

where Γ is the sRGB transfer function [16].

mSDF supervision. Since all pixels with $M_{\text{GT}} = 0$ should have a non-positive projected mSDF value we introduce the following loss on mSDF values:

$$L_{\text{mSDF}} = \|(M_{\nu} - M_{\text{GT}})_+ \odot \text{sgn}(1 - M_{\text{GT}})\|_1, \quad (6)$$

in which M_{ν} is the rendered (*i.e.*, projected) mSDF image.

Optionally, one may pay extra memory and time to render render an mSDF image $M_{\nu, \text{watertight}}$ from the watertight template mesh (by setting mSDF values to 1). Since all pixels with $M_{\text{GT}} = 1$ should possess a positive mSDF value, we may have the following additional loss

$$L_{\text{mSDF, watertight}} = \|(M_{\nu, \text{watertight}} - M_{\text{GT}})_+ \odot \text{sgn}(M_{\text{GT}})\|_1. \quad (7)$$

Depth supervision. In cases when ground truth depth images are provided, we include a depth supervision loss:

$$L_{\text{Depth}} = \|I_{\text{Depth, rendered}} - I_{\text{Depth, GT}}\|_1. \quad (8)$$

Eikonal regularization. To reconstruct smoother surfaces, we use the standard Eikonal regularization [13] for MLP-parameterized SDF values on the vertices of the reconstructed mesh:

$$L_{\text{Eikonal}} = (\|\nabla f_{\theta}(x)\|_2 - 1)^2. \quad (9)$$

mSDF regularization. We rewrite the mSDF regularization, introduced in the main paper, into the following (with $\epsilon = 0.001$):

$$L_{\text{mSDF-reg-open}}(\theta_{\text{mSDF}}) = \sum_{u: \nu_{\theta}(u) \geq 0} L_{\text{huber}}(\nu_{\theta}(u)), \quad (10)$$

$$L_{\text{mSDF-reg-close}}(\theta_{\text{mSDF}}) = \sum_{\substack{u': \nu_{\theta}(u')=0 \\ u' \text{ visible from some } q \in Q}} L_{\text{huber}}(\nu_{\theta}(u') - \epsilon). \quad (11)$$

Determine if a mesh vertex u' is visible for the set of all training camera poses is computationally costly. Therefore, we instead use an approximated loss for $L_{\text{mSDF-reg-close}}$:

$$L_{\text{mSDF-reg-close}}(\theta_{\text{mSDF}}) = \sum_{\substack{u': \nu_{\theta}(u')=0 \\ u' \text{ visible from some } q \in Q_t}} L_{\text{huber}}(\nu_{\theta}(u') - \epsilon). \quad (12)$$

in which Q_t is the batch of camera poses at training iteration t .

Note that we stop the gradient flow from these two losses to both SDF and grid vertex offsets. While it is possible to allow gradients from mSDF regularization to update SDF and grid vertex offsets as well, we choose not to do so to stabilize the optimization process.

We follow [16] and use the following regularization losses:

Albedo smoothness regularization. To effectively decouple light from material, smoothness regularization is imposed on albedo k_d :

$$L_{k_d} = \frac{1}{x_{\text{surf}}} \sum_{x_{\text{surf}}} |k_d(x_{\text{surf}}) - k_d(x_{\text{surf}} + \epsilon_{k_d})|, \quad (13)$$

in which $\epsilon_{k_d} \sim \mathcal{N}(0, \sigma_{k_d}^2)$ (we use $\sigma_{k_d} = 0.01$).

SDF regularization. The following SDF regularization is to reduce floaters and inner geometry:

$$L_{\text{SDF-reg}} = \sum_{i,j \in S} H(\sigma(s_i), \text{sgn}(s_j)) + H(\sigma(s_j), \text{sgn}(s_i)) \quad (14)$$

where S is the set of unique edges on the 3D grid, H is the binary cross-entropy loss, s_i, s_j are the SDF values of the corresponding grid vertices and sgn is the sign function.

Monochrome regularization. The following loss⁶ helps decoupling lighting, geometry and material:

$$L_{\text{light}} = \|T(Y(c_d + c_s)) - T(V(I_{\text{ref}}))\|_1 \quad (15)$$

where c_d and c_s are the diffuse and specular light components, I_{ref} is the target reference image, T is the tonemapping function introduced earlier, $Y(x)$ is the simple luminance operator by averaging RGB channels $(x_r + x_g + x_b)/3$, and $V = \max(x_r, x_g, x_b)$.

In addition, we penalize the specular component with the following loss:

$$L_{\text{specular}} = \frac{\lambda_{\text{specular}} \|Y(c_s)\|_1}{\min\{\|Y(c_d)\|_1, \epsilon\}}. \quad (16)$$

Mesh topology regularization. Finally, for the **G-SHELL** variant with FlexiCubes, we follow [51] and use the proposed mesh topology regularization L_{dev} which penalizes mean absolute deviation between the primal and dual vertices in FlexiCubes. The precise loss and parameter definitions are beyond the scope of the paper and we do not elaborate them here.

Total loss. In summary, the total loss is

$$L_{\text{Total}} = L_{\text{rendering}} + L_{\text{geometry-reg}} + L_{\text{material-light-reg}} \quad (17)$$

with

$$\begin{aligned} L_{\text{rendering}} &= L_{\text{RGB}} + \gamma_{\text{Mask}} L_{\text{Mask}} + \gamma_{\text{Depth}} L_{\text{Depth}} \\ &\quad + \gamma_{\text{mSDF}} L_{\text{mSDF}} + \gamma_{\text{mSDF, watertight}} L_{\text{mSDF, watertight}}, \end{aligned} \quad (18)$$

$$\begin{aligned} L_{\text{geometry-reg}} &= \gamma_{\text{Eikonal}} L_{\text{Eikonal}} + \gamma_{\text{SDF-reg}} L_{\text{SDF-reg}} \\ &\quad + \gamma_{\text{mSDF-reg-open}} L_{\text{mSDF-reg-open}} + \gamma_{\text{mSDF-reg-close}} L_{\text{mSDF-reg-close}} \\ &\quad + \gamma_{\text{dev}} L_{\text{dev}}, \end{aligned} \quad (19)$$

and

$$L_{\text{material-light-reg}} = \gamma_{\text{light}} L_{\text{light}} + \gamma_{\text{specular}} L_{\text{specular}} + \gamma_{k_d} L_{k_d}. \quad (20)$$

Choice of loss scales. For DeepFashion3D instances, we set $\gamma_{\text{Mask}} = 1$, $\gamma_{\text{mSDF}} = 0.5$, $\gamma_{\text{mSDF-reg-close}} = 10^{-6}/\rho$, $\gamma_{\text{mSDF-reg-open}} = 3 \times 10^{-6}/\rho$, $\gamma_{\text{mSDF, watertight}} = 0$, $\gamma_{\text{light}} = 0.15$ and $\gamma_{\text{specular}} = 0.0025$, where $\rho = (\text{grid-resolution}/64)^3$. We use a linear schedule for Eikonal regularization: $\gamma_{\text{Eikonal}} = 0.3$ for

⁶There are slight differences between the Nvdiffrccmc paper, the official repository of Nvdiffrccmc and our implementation. Please see Sec. B.2 for more details.

the first 500 iterations, $\gamma_{\text{Eikonal}} = 0.1$ for iteration 500 to 2000 and $\gamma_{\text{Eikonal}} = 0.01$ for the remaining iterations.

For the synthetic chair experiment, we set $\gamma_{\text{mSDF, watertight}} = 0.1$, $\gamma_{\text{Eikonal}} = 5e - 3$, $\gamma_{\text{mSDF-reg-close}} = 2e - 4/\rho$. We set $\gamma_{\text{mSDF-reg-open}}$ to $2e - 5/\rho$ for the first 1500 iterations and $2e - 6/\rho$ for the remaining ones.

We set $\gamma_{\text{dev}} = 0.25$ for the **G-SHELL** variant with FlexiCubes but otherwise 0.

All other loss scales not mentioned are set to default values as in [16].

B.2 DIFFERENCES IN IMPLEMENTATIONS FOR LIGHTING REGULARIZATION

We note the difference between the Nvdiffrccmc paper [16] and the official implementation⁷. In the original paper, the lighting regularization is written such that T is the first to be applied to the rendered and reference image:

$$\|Y(T(c_d + c_s)) - V(T(I_{\text{ref}}))\|_1. \quad (21)$$

The official implementation uses a modified regularization loss, in which the first term tends to encourage specular components ($\epsilon = 0.001$ in the repo):

$$\lambda_{\text{diffuse}} \frac{\|Y(c_d)\|_1}{\min\{\|Y(c_d + c_s)\|_1, \epsilon\}} \|T(Y(c_d + c_s)) - I_{\text{ref}}\|_1 + \frac{\lambda_{\text{specular}} \|Y(c_s)\|_1}{\min\{\|Y(c_d)\|_1, \epsilon\}}. \quad (22)$$

B.3 RENDERING, OPTIMIZATION AND OTHER SETTINGS

For **G-SHELL** with tetrahedral grids, we set the number of rays samples of the Nvdiffrccmc renderer (for Monte-Carlo approximation of the rendering equation) $N_{\text{sample}} = 24$ for better performance on the interior of meshes (*e.g.*, clothing in DeepFashion3D dataset). In practice, setting $N_{\text{sample}} = 12$ leads to faster convergence (approx. 2 hours) without too much sacrifice on reconstruction quality (PSNR values lowered by less than 1). For **G-SHELL** with FlexiCubes, we instead use $N_{\text{sample}} = 16$.

As occlusion heavily depends on shape topology, it will be hard to optimize both lighting and shape topology at the same time with some initialized shape. To alleviate this issue, we follow [16] and use soft occlusion during the first few hundred iterations. Specifically, the occluded light rays will be scaled by η , which gradually decreases from 1 at iteration 0 to 0 at iteration 1000. Please refer to [16] for implementation details.

The learnable PBR materials are parameterized in the same way as in [16]. We do not learn a normal map (and therefore the normal regularization in the Nvdiffrccmc paper does not apply here).

We use Adam optimizer with $(\beta_1, \beta_2) = (0.9, 0.99)$. The total number of iterations for each shape is 5000. The initial learning rate of the MLP for parameterizing SDF values is set to $3e - 4$ while those for mSDF and grid vertex offsets are set to 0.15. The initial learning rate for the rest of parameters used in **G-SHELL** with FlexiCubes are set to $3e - 4$. The learning rates follow a decay schedule of $10^{-0.0002 \cdot t}$ where t is the iteration number.

We use an MLP with 6 hidden layers and a hidden channel size of 128 (with a concatenation shortcut from input to the output of the 4th layer) to parameterize SDFs. We use the standard positional encoding (for instance in [40]): $[1, \cos(2^1x), \sin(2^1x), \cos(2^2x), \sin(2^2x), \dots, \cos(2^Kx), \sin(2^Kx)]$ with $K = 6$. We use Softplus activation with $\beta = 100$ for all layers except for the final output layer (in which no activation function is used). The MLP is initialized by fitting the SDF of a sphere.

The learnable grid vertex offsets, after multiplied by the scale of deformation, are directly added to the canonical (*i.e.*, undeformed) grid vertex positions. After each gradient update, we clip the learned (and unscaled) grid vertex offsets to $[-1, 1]$. These learnable offsets are initialized to 0.

The images for the DeepFashion3D ground truth shapes are rendered using Cycles engine in Blender with 5,000 samples, a number of max bounces of 24 and a fixed environment lightmap.

We sample 100,000 points per mesh to compute Chamfer distances. Here we use the implementation in ECON [58]⁸, which computes the bi-directional metric with pointcloud-to-surface distances.

⁷<https://github.com/NVlabs/nvdiffrccmc>

⁸<https://github.com/YuliangXiu/ECON/blob/master/lib/dataset/Evaluator.py>

C DETAILED SETTINGS ON DIFFUSION MODELS WITH G-SHELL

C.1 GRID STORAGE OF INTERPOLATION COEFFICIENTS FROM mSDF

As described in the main paper, in each tetrahedral cell there are 12 candidate (watertight) mesh edges if we count all possible SDF configurations. Since these 12 candidate edges are in general spatially separated, we take the simplest approach and store them on a larger cubic grid.

Suppose (normalized) SDF values and grid vertex offsets are stored in a cubic grid of resolution R , the same as in MeshDiffusion. Due to the spatial regularity of these 12 candidate edges (as long as we use a regular enough tetrahedral grid), we design a positional embedding for each edge. Specifically, the “location” of each candidate edge (u_i, u_j) , of which u_i lies on the tetrahedral grid edge (p_1, p_2) and u_j on (p_2, p_3) , is

$$\frac{\bar{p}_1 + \bar{p}_3 + 2\bar{p}_2}{4} \quad (23)$$

where \bar{p} ’s are the undeformed grid vertices respectively. With these positional embeddings, we may store them to the nearest coordinate in a larger cubic grid of resolution $2R$. As a result, we are able to use 3D U-Net for a diffusion model to jointly generate SDF values, deformation vectors and mSDF-induced interpolation coefficients.

For each candidate edge (u_i, u_j) , we may either generate α_i or α_j (note that $\alpha_j = 1 - \alpha_i$). We pick the simplest convention: we first sort two nodes (u_i, u_j) of each candidate edge in a lexicographical order of the three dimensions of a and b , and then for each sorted edge (a, b) , we always pick α_a as the interpolation coefficient to generate.

C.2 ARCHITECTURE AND TRAINING SETTINGS

We use the same architecture of MeshDiffusion but add two input layers (one for the mSDF values and one for the mSDF grid mask which indicates where in the grid stores mSDF values; each implemented with a 3D convolution layer of kernel size 3) and an output layer (implemented with a transposed 3D convolution layer with kernel size 4, stride 2 and padding 1) to accommodate the introduction of an additional grid for mSDF-induced interpolation coefficients. The output of the additional input layer is directly added to the output of the original input layer in the MeshDiffusion U-Net architecture. Similar to MeshDiffusion, the predicted mSDF noise is multiplied by the mSDF grid mask so that only the used mSDF grid locations are counted.

We follow the training settings in MeshDiffusion with a reduced learning rate of $1e - 5$. We use a batch size of 8 with 4 gradient accumulation steps (with 8 80GB-mem A100 GPUs). We use mixed precision training to speed up the training process.

C.3 DATA PREPARATION

We use the official GET3D implementation⁹ to prepare datasets of rendered images for ground truth meshes (with a simple diffuse-only material). For MeshDiffusion (with DMTet), we mostly follow [35] but fit each object with 1000 iterations for both coarse-fitting and finetuning stages (instead of 5000) with the deformation scales set to 0 and 2.0, respectively. For G-MeshDiffusion, we use the depth supervision loss with $\gamma_{\text{depth}} = 100$ but disable the mSDF regularization losses as the depth information is enough for identifying topological holes on ground truth shapes. As in the reconstruction experiments, SDFs are parameterized by an MLP instead of being directly stored as learnable scalars in the tetrahedral grid. We recenter the meshes to the origin (in the world coordinate), and then rescale all meshes in an isotropic way so that the minimum and maximum of the bounding box coordinates are -1 and 1 , respectively. After rescaling, we compute the minimum and maximum of x, y, z coordinates in each dataset (upper and lower garments) and scale the tetrahedral grid with $H = (0.45(x_{\max} - x_{\min}), 0.45(y_{\max} - y_{\min}), 0.45(z_{\max} - z_{\min}))$. The SDF values are initialized to fit a ellipsoid obtained by scaling a unit sphere with H . The mSDF values stored on tetrahedral grids are initialized in the same way as in reconstruction experiments: we randomly initialize them by sampling from a uniform distribution $\mathcal{U}(-0.01, 0.99)$.

⁹<https://github.com/nv-tlabs/GET3D>

D MORE QUALITATIVE EXAMPLES OF MULTI-VIEW MESH RECONSTRUCTION

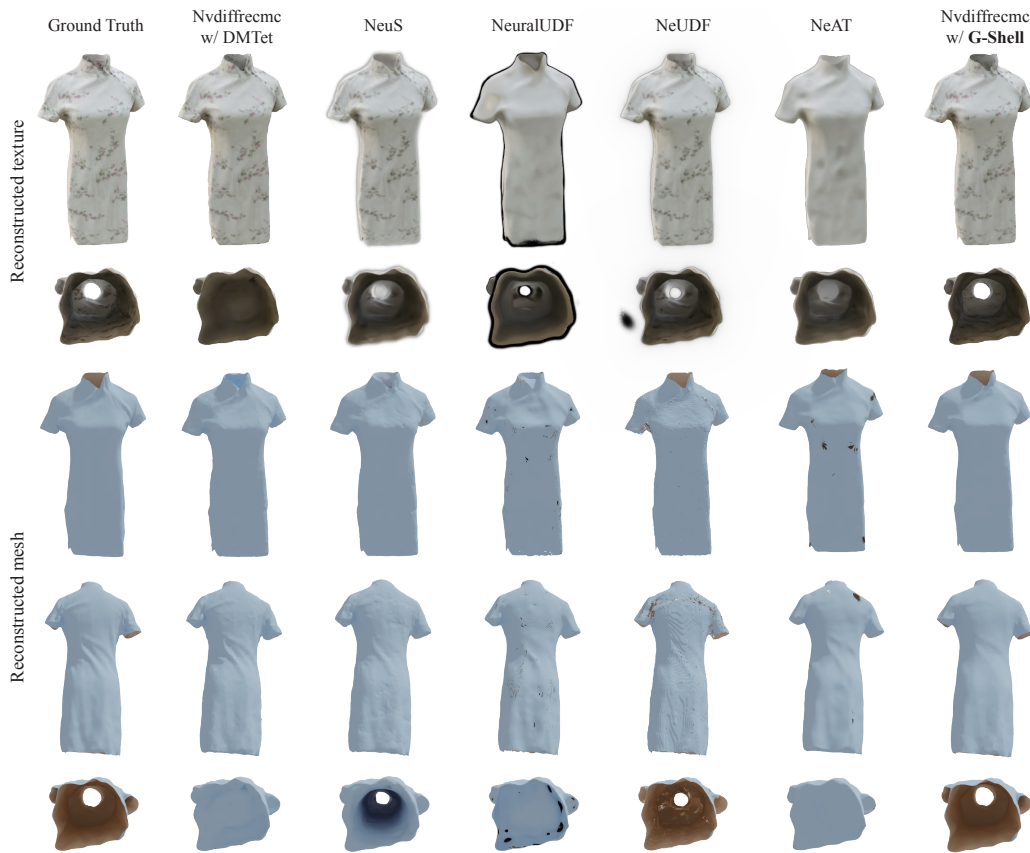


Figure 11: Comparison between reconstruction w/ **G-SHELL** and baseline methods on instance 92 in DeepFashion3D dataset.

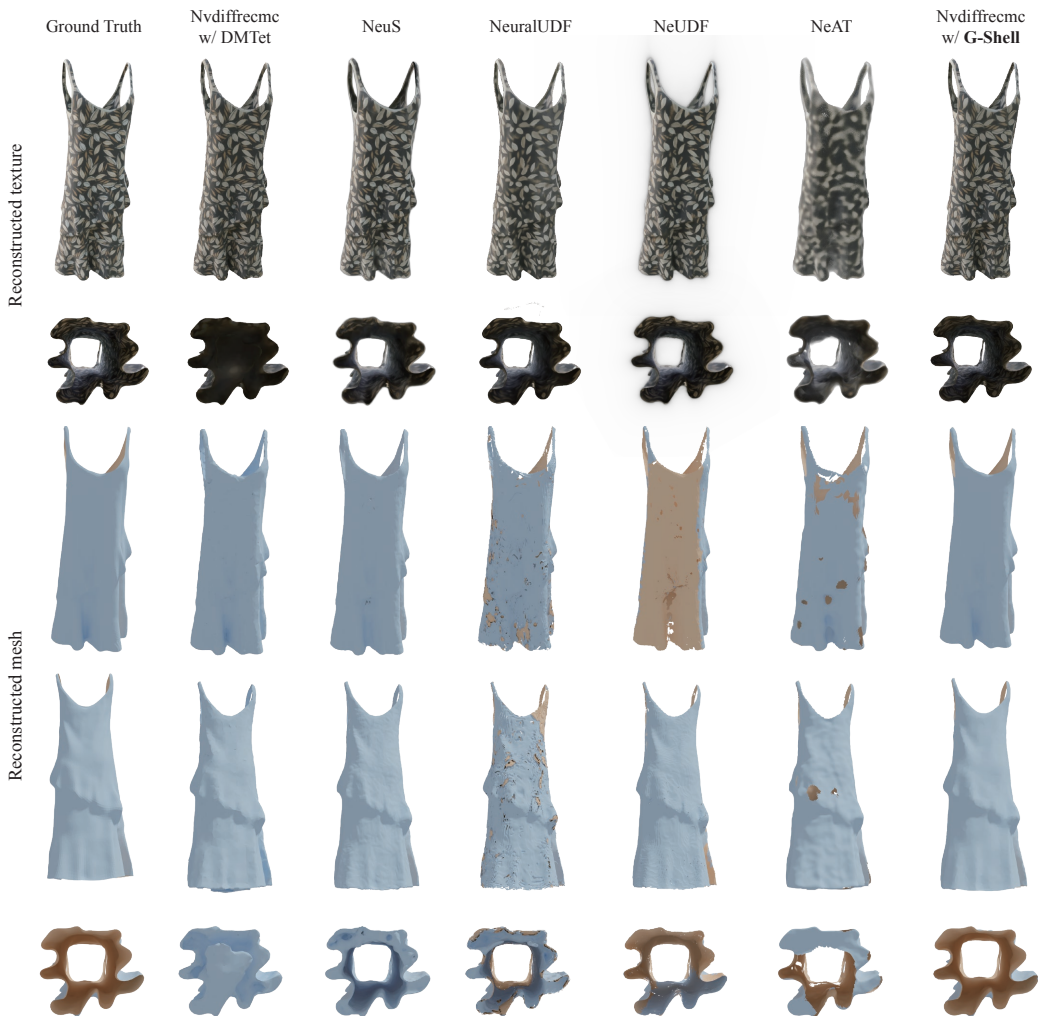


Figure 12: Comparison between reconstruction w/ **G-SHELL** and baseline methods on multiview reconstruction on instance 117 in DeepFashion3D dataset.



Figure 13: Comparison between reconstruction w/ **G-SHELL** and baseline methods on multiview reconstruction on instance 320 in DeepFashion3D dataset.

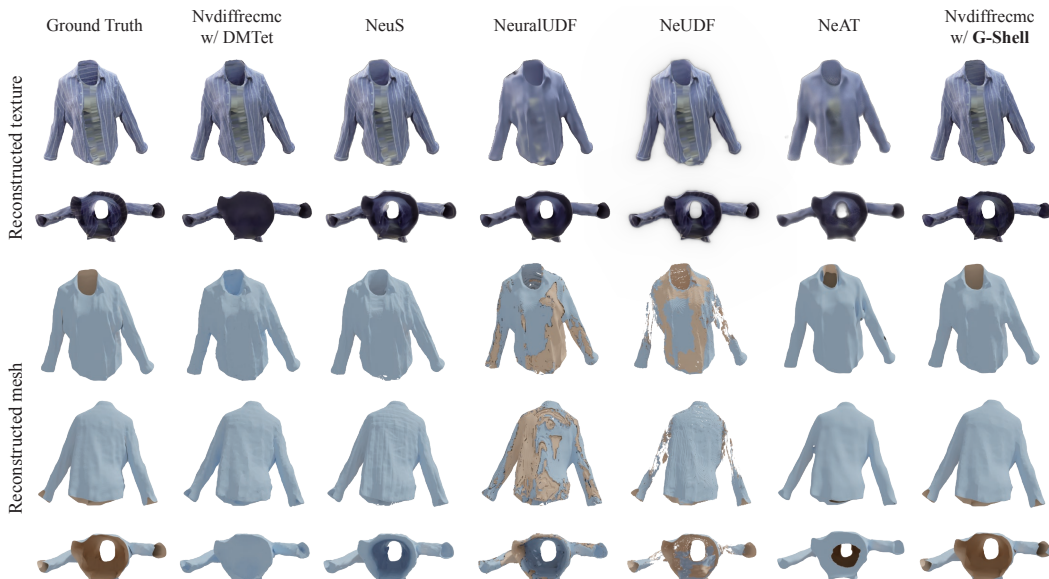


Figure 14: Comparison between reconstruction w/ **G-SHELL** and baseline methods on multiview reconstruction on instance 522 in DeepFashion3D dataset.

E RECONSTRUCTED MESHES FOR SURFACES WITH COMPLEX PATTERNS

We also show the reconstruction result of a non-watertight surface with complex surface patterns in Figure 15. The results show that **G-SHELL** can almost perfectly reconstruct the geometry.

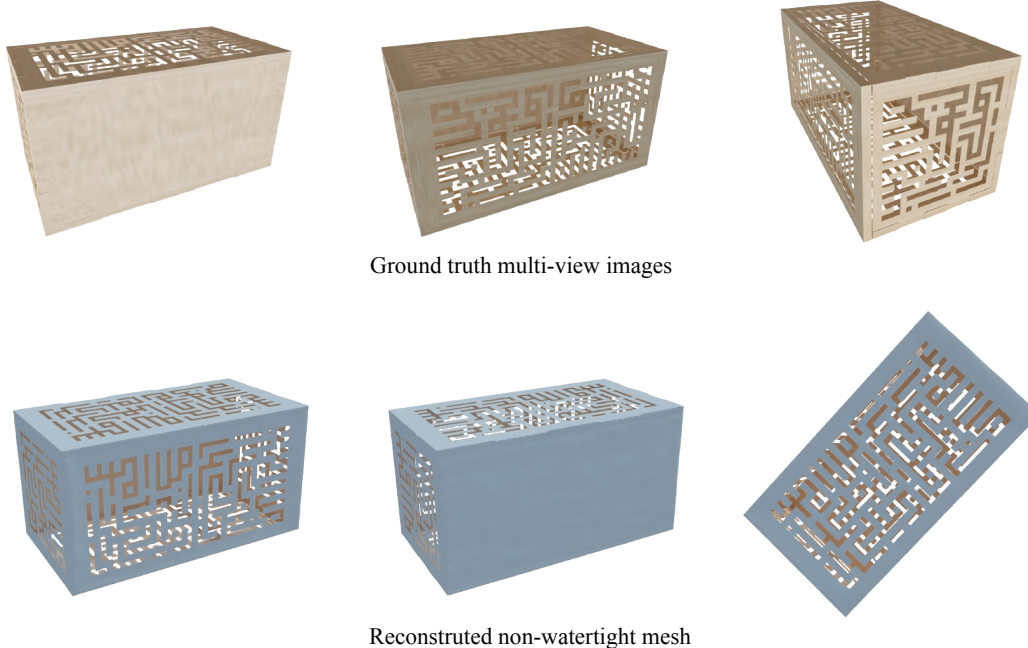


Figure 15: Reconstruction results of a non-watertight surface with complex surface patterns from multi-view images.

F RECONSTRUCTION OF SHAPES WITH METALLIC MATERIALS

We visualize the ground truth and reconstructed shape in the specular lighting setting. With the increase of metalness in the material, the reconstructed shapes start to contain artifacts. Yet the reconstructed 3D meshes still replicate most of the target geometry and texture. The missing specular lighting effect in the rendered image is mostly due to the limitation of the renderer – no indirect illumination is considered. More advanced differentiable rendering methods may solve this issue.

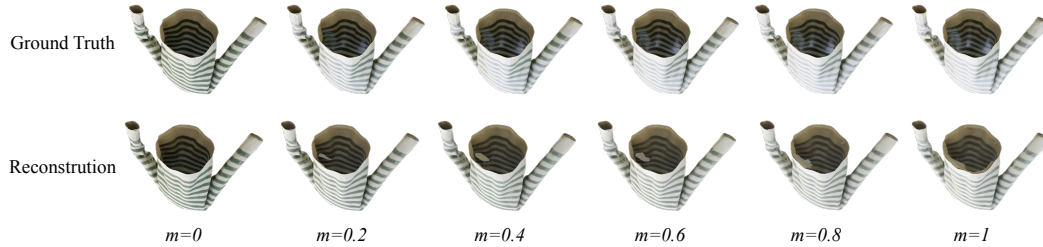


Figure 16: Qualitative results of the ablation study on the change of specular parameter in the ground truth mesh material. m represents metalness parameter.

G ON MSDF REGULARIZATION

It might be tempting to ignore the second term the mSDF regularization loss with some well-tuned set of loss coefficients. However, we empirically observe that it is hard to find a good choice for $\gamma_{\text{mSDF-reg-open}}$ to achieve conservative yet effective hole opening regularization. A too large $\gamma_{\text{mSDF-reg-open}}$ typically results in large topological holes when the shape to optimize is still far from the target shape, while a too small value fails to create topological holes when needed. It is possible to find a schedule of $\gamma_{\text{mSDF-reg-open}}$ without $L_{\text{mSDF-reg-close}}$. However, we note that the schedule of $\gamma_{\text{mSDF-reg-open}}$ has to synchronize with the schedule of shadow ray contribution: once the occluded light rays hardly contribute in rendered colors, it is in general hard for the shape topology to change. A time-invariant loss coefficient of $L_{\text{mSDF-reg-close}}$ is in general easier to control and more robust.